sensors

MDPI

Article

# Multiple Temperature-Sensing Behavior of Green and Red Upconversion Emissions from Stark Sublevels of $Er^{3+}$

**Baosheng Cao, Jinlei Wu, Xuehan Wang, Yangyang He, Zhiqing Feng and Bin Dong ***

Received: 7 September 2015; Accepted: 1 December 2015; Published: 10 December 2015
Academic Editor: Vittorio M. N. Passaro

School of Physics and Materials Engineering, Dalian Nationalities University, Dalian 116600, China;
bscao@dlnu.edu.cn (B.C.); mrwu888@live.cn (J.W.); xhanwang@tom.com (X.W.); yyhe@dlnu.edu.cn (Y.H.);
fzq@dlnu.edu.cn (Z.F.)
* Correspondence: dong@dlnu.edu.cn; Tel.: +86-411-87656135; Fax: +86-411-87656331

**Abstract:** Upconversion luminescence properties from the emissions of Stark sublevels of $Er^{3+}$ were investigated in $Er^{3+}$-$Yb^{3+}$-$Mo^{6+}$-codoped $TiO_2$ phosphors in this study. According to the energy levels split from $Er^{3+}$, green and red emissions from the transitions of four coupled energy levels, $^2H_{11/2(I)}/^2H_{11/2(II)}$, $^4S_{3/2(I)}/^4S_{3/2(II)}$, $^4F_{9/2(I)}/^4F_{9/2(II)}$, and $^2H_{11/2(I)}$ + $^2H_{11/2(II)}/^4S_{3/2(I)}$ + $^4S_{3/2(II)}$, were observed under 976 nm laser diode excitation. By utilizing the fluorescence intensity ratio (FIR) technique, temperature-dependent upconversion emissions from these four coupled energy levels were analyzed at length. The optical temperature-sensing behaviors of sensing sensitivity, measurement error, and operating temperature for the four coupled energy levels are discussed, all of which are closely related to the energy gap of the coupled energy levels, FIR value, and luminescence intensity. Experimental results suggest that $Er^{3+}$-$Yb^{3+}$-$Mo^{6+}$-codoped $TiO_2$ phosphor with four pairs of energy levels coupled by Stark sublevels provides a new and effective route to realize multiple optical temperature-sensing through a wide range of temperatures in an independent system.

**Keywords:** temperature sensing; upconversion emissions; Stark sublevel; rare earth; sensitivity

## 1. Introduction

Optical temperature-sensing devices have been widely researched to promote their application in electrical power stations, oil refineries, coal mines, and fire detection, as they have been shown to overcome the interference of strong electromagnetic noise, hazardous sparks, or corrosive environments inaccessible to traditional temperature-measurement methods such as thermocouple detectors [1–5]. Sensors built based on the fluorescence intensity ratio (FIR) technique have attracted particular attention due to their ability to reduce dependence on measurement conditions and improve accuracy and resolution. FIR functions independent of fluorescence loss or fluctuations in excitation intensity can be applied to fluorescence systems in which two closely spaced energy levels with separations of the order of thermal energy are involved, following a Boltzmann-type population distribution [1,6,7]. Optical temperature sensors using the FIR technique are mainly focused on fluoride and oxides matrixes [8–14]. The fluoride matrixes possesses higher fluorescence efficiency and lower excitation power; however, the maximum operating temperature is usually low. On the contrary, the oxides matrices can operate at high temperature, although the fluorescence intensity is lower.

Upconversion emissions of rare earth ion-doped materials are typically utilized to realize FIR measurement because of the large amount of coupled energy levels in many rare earth ions and the easily accessible upconversion luminescence with near-infrared radiation from low-cost, commercially available diodes. Xu *et al.* [8], for example, reported the FIR of $Ho^{3+}$ using two blue emissions from coupled energy levels of $^5G_6/^5F_1$ and $^5F_{2,3}/^3K_8$ and found that $Ho^{3+}$-$Yb^{3+}$-codoped $CaWO_4$ possessed higher absolute sensitivity due to a larger energy gap between the thermally coupled $^5G_6/^5F_1$ and $^5F_{2,3}/^3K_8$ levels of $Ho^{3+}$ ions. The paired energy levels of $^3F_2$ and $^3F_3$ in $Tm^{3+}$ ions have also been used to investigate temperature-dependent red upconversion emissions and corresponding FIR properties [9]. The FIR properties of green upconversion emissions ascribed to paired energy levels of $^2H_{11/2}$ and $^4S_{3/2}$ in $Er^{3+}$-doped materials, in particular, have been quite widely studied [10–14].

In addition to the intrinsic thermally coupled energy levels of rare earth ions, the pair energy levels of Stark sublevels can also be thermally coupled and used to investigate FIR *versus* temperature characteristics [15–18]. Baxter *et al.* [17], for example, used the coupled energy levels of $^2F_{5/2(a)}$ and $^2F_{5/2(b)}$ by Stark split of $^2F_{5/2}$ levels in $Yb^{3+}$ ions to study FIR properties of $Yb^{3+}$-doped silica fiber. Feng *et al.* [18] investigated the FIR properties of $Er^{3+}$-doped fluoride glass using coupled Stark sublevels of $^4S_{3/2(1)}$ and $^4S_{3/2(2)}$ in $Er^{3+}$ ions.

In this study, four thermally coupled energy levels of $Er^{3+}$ ions based on the Stark sublevels were simultaneously observed in $Er^{3+}$-$Yb^{3+}$-$Mo^{6+}$-codoped $TiO_2$ phosphors. FIR properties of the four coupled energy levels from green and red emissions in $Er^{3+}$-$Yb^{3+}$-$Mo^{6+}$-codoped $TiO_2$ phosphors were studied as a function of temperature in the range of 307–673 K. The effects of the energy gap of thermally coupled energy levels, FIR value, and upconversion emission intensity on the sensitivity and accuracy of the optical temperature sensor are discussed in an effort to explore potential developments in optical temperature-sensor technology based on different FIR routes in an independent system.

## 2. Experimental Section

The sol-gel method was used to prepare $Er^{3+}$-$Yb^{3+}$-$Mo^{6+}$-codoped $TiO_2$ phosphors. The rare earth nitrates $Er(NO_3)_3 \cdot 5H_2O$ (99.99%) and $Yb(NO_3)_3 \cdot 5H_2O$ (99.99%) were purchased from Aladdin. Other chemicals including Iso-Propanol (i-PrOH), *n*-butyl titanate ($Ti(OBu)_4$), acetylacetone (AcAc), and concentrated nitric acid ($HNO_3$) were purchased from Sinopharm Chemical Reagent Co., Ltd. (Shanghai, China). All chemicals are of analytical reagent and were used without any further purification. i-PrOH was first added as a solvent to modified titanium(IV) *n*-butoxide by facilitating a chelating reaction between $Ti(OBu)_4$ and AcAc under agitation for 1 h at room temperature. Next, a mixture of deionized water, i-PrOH, and $HNO_3$ was slowly added into the solution. The mixed solution was stirred for 6 h to form a clear and stable sol. The molar ratios of $Ti(OBu)_4$, AcAc, $H_2O$, and $HNO_3$ were 3:3:6:1. Finally, Er, Mo, and Yb ions were introduced by adding $Er(NO_3)_3 \cdot 5H_2O$, $(NH_4)_6Mo_7O_{24} \cdot 5H_2O$, and $Yb(NO_3)_3 \cdot 5H_2O$ in the molar ratio of 2:2:20:100 for Er:Mo:Yb:Ti. The codoped sols were dried at 373 K for 8 h to remove the solvent. The xerogels were then heated at a rate of 4 K/min and maintained at the sintering temperature of 1073 K for 1 h, then cooled to room temperature in the furnace. The sintered 2 mol % $Er^{3+}$–20 mol % $Yb^{3+}$–2 mol % $Mo^{6+}$-codoped $TiO_2$ phosphors were finally milled into powders for structural analysis and spectral measurement.

The phase structures of $Er^{3+}$-$Yb^{3+}$-$Mo^{6+}$-codoped $TiO_2$ phosphor samples were analyzed by SHIMADZU XRD-6000 X-ray diffractometer (XRD) with Cu-K$\alpha$ radiation. A homemade temperature control system, which was composed of a small stove and an intelligent digital-display-type temperature control instrument, was used to adjust sample temperature from 307 to 673 K, at measurement and control accuracy of about ±0.5 K. Temperature-dependent upconversion emissions from each sample were focused onto a Jobin Yvon iHr550 monochromator and detected with a CR131 photomultiplier tube by 976 nm laser diode (LD) excitation. The LD pump current varied from 0 to 2 A, and the spectral resolution of the experimental set-up was 0.1 nm.

## 3. Results and Discussion

Figure 1 shows XRD patterns of the $Er^{3+}$-$Yb^{3+}$-$Mo^{6+}$-codoped $TiO_2$ phosphor samples. The XRD pattern observed was characteristic of the anatase phase of $TiO_2$ (JCPDS No. 21-1272) and the face-centered cubic phase of $Yb_2Ti_2O_7$ (JCPDS No. 17-0454) referenced below. There was no diffraction peak of Mo compounds, and the main diffraction peak shifted toward small angles, indicating $Mo^{6+}$ stochastically located at the interstitial sites of the matrix lattice as a solution element.

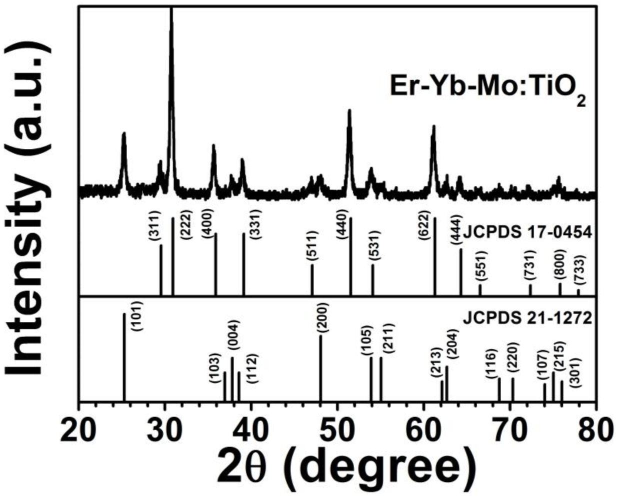

**Figure 1.** XRD pattern of $Er^{3+}$-$Yb^{3+}$-$Mo^{6+}$ codoped $TiO_2$.

Figure 2 shows the upconversion emission spectra of $Er^{3+}$-$Yb^{3+}$-$Mo^{6+}$-codoped $TiO_2$ under different pump currents. Green and red upconversion emissions were observed in the wavelengths of 500–540 nm, 540–580 nm, and 620–710 nm, corresponding to $^{2}H_{11/2}\rightarrow$ $^{4}I_{15/2}$, $^{4}S_{3/2}\rightarrow$ $^{4}I_{15/2}$, and $^{4}F_{9/2}\rightarrow$ $^{4}I_{15/2}$ transitions of $Er^{3+}$ ions, respectively. Each transition ($^{2}H_{11/2}\rightarrow$ $^{4}I_{15/2}$, $^{4}S_{3/2}\rightarrow$ $^{4}I_{15/2}$, and $^{4}F_{9/2}\rightarrow$ $^{4}I_{15/2}$) was divided into two emission peaks, which indicated $^{2}H_{11/2}$, $^{4}S_{3/2}$, and $^{4}F_{9/2}$ levels of $Er^{3+}$ split into three coupled Stark sublevels of $^{2}H_{11/2(I)}\cdot$ ($H_I$) and $^{2}H_{11/2(II)}\cdot$ ($H_{II}$), $^{4}S_{3/2(I)}\cdot$ ($S_I$) and $^{4}S_{3/2(II)}\cdot$ ($S_{II}$), and $^{4}F_{9/2(I)}\cdot$ ($F_I$) and $^{4}F_{9/2(II)}\cdot$ ($F_{II}$), respectively, due to the effect of crystal field environment on $Er^{3+}$ ions. As the LD pump current increased from 0.8 to 2.0 A, the position and number of upconversion emission peaks did not change, whereas the intensity of green and red emissions markedly increased due to the increase in excitation power.

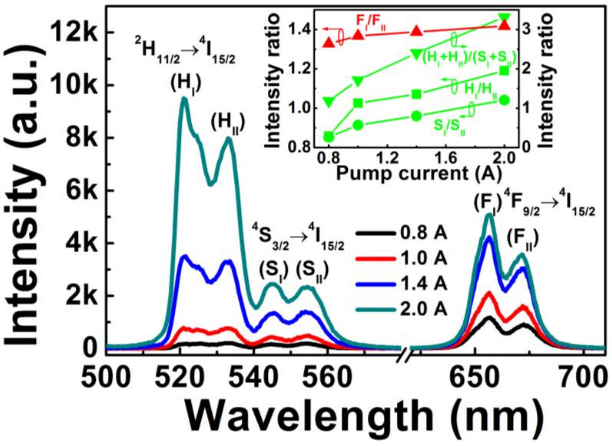

**Figure 2.** Upconversion emissions spectra of $Er^{3+}$-$Yb^{3+}$-$Mo^{6+}$-codoped $TiO_2$ with different pump currents. Inset shows corresponding upconversion emission intensity ratios *versus* the pump current.

The inset in Figure 2 shows the upconversion emission intensity ratios of $H_I/H_{II}$, $S_I/S_{II}$, $F_I/F_{II}$, and $(H_I + H_{II})/(S_I + S_{II})$ *versus* the pump current. All intensity ratios of $H_I/H_{II}$, $S_I/S_{II}$, $F_I/F_{II}$ and $(H_I + H_{II})/(S_I + S_{II})$ increased alongside the pump current, implying that the nonradiative processes of $Er^{3+}$ in $Er^{3+}$-$Yb^{3+}$-$Mo^{6+}$-codoped $TiO_2$ phosphor can partially transform pump energy into heat energy, therefore elevating the phosphor temperature. The temperature variation induced by increasing the pump current caused changes in the intensity ratio [19]; this suggests that the temperature-dependent intensity ratio for the four coupled energy levels of $H_I/H_{II}$, $S_I/S_{II}$, $F_I/F_{II}$, and $(H_I + H_{II})/(S_I + S_{II})$ can be utilized for optical temperature sensing.

Figure 3 shows a schematic energy level diagram of the $Er^{3+}$-$Yb^{3+}$-$Mo^{6+}$-codoped $TiO_2$ phosphors under 976 nm LD excitation. The upconversion mechanism of $Er^{3+}$ after the addition of $Mo^{6+}$ was reported in a previous study on the sensitization of the $Yb^{3+}$-$MoO_4{}^{2-}$ dimer to $Er^{3+}$ [20–22]. Through a cooperative sensitization process in the $Yb^{3+}$-$MoO_4{}^{2-}$ dimer, two excited $Yb^{3+}$ ions nonradiatively transfer their energy to $MoO_4{}^{2-}$. This process is followed by a high excited state energy transfer (HESET) to the $^4F_{7/2}$ level of $Er^{3+}$ ions. After nonradiative relaxations from $^4F_{7/2}$ to the Stark sublevels of $H_I$, $H_{II}$, $S_I$ and $S_{II}$, green upconversion emissions are produced by transitions of $H_I/H_{II}/S_I/S_{II} \rightarrow {}^4I_{15/2}$. The nonradiative relaxation from $S_{II}$ to $F_I$ and $F_{II}$ levels and subsequent transitions of $F_I/F_{II} \rightarrow {}^4I_{15/2}$ generate red emissions.

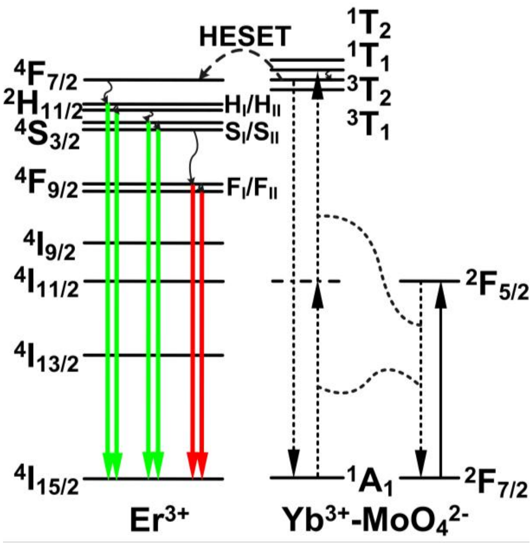

**Figure 3.** Schematic energy level diagram of $Er^{3+}$-$Yb^{3+}$-$Mo^{6+}$-codoped $TiO_2$ phosphors under 976 nm LD excitation. Wavy arrows indicate nonradiative relaxation.

In order to distinguish the effects of temperature from the pump current on the intensity ratio (Figure 2), the upconversion emission properties of $Er^{3+}$-$Yb^{3+}$-$Mo^{6+}$-codoped $TiO_2$ were measured under different temperatures. Figure 4 shows the upconversion emissions spectra of $Er^{3+}$-$Yb^{3+}$-$Mo^{6+}$-codoped $TiO_2$ at measured temperatures between 307 and 673 K. Changes in temperature had no influence on the bands of green and red emissions from $^2H_{11/2}/{}^4S_{3/2} \rightarrow {}^4I_{15/2}$ and $^4F_{9/2} \rightarrow {}^4I_{15/2}$ transitions of $Er^{3+}$ between 500 to 580 nm and 620 to 700 nm, respectively; the intensity varied with temperature, however. The inset in Figure 4 shows the intensity of green and red emissions and the intensity ratio of green to red emissions as a function of temperature. The intensity of red emissions decreased with increasing temperature, in accordance with the classical theory of thermal quenching. Temperature-dependent intensity of the red emissions can be expressed as follows [23]:

$$I(T) = \frac{I(0)}{1 + A\exp\left(-\Delta E'/kT\right)} \tag{1}$$

where $T$ is the absolute temperature, and $I(T)$ and $I(0)$ are the fluorescence intensities at temperatures of $T$ and 0 K, respectively; $\Delta E'$ is the activation energy, $k$ is the Boltzmann constant, and $A$ is a constant. The temperature-dependent intensity of red emissions fits well to Equation (1), where $\Delta E'_{(\mathrm{FI+FII})}$ = 0.074 eV.

Conversely, the intensity of green emissions increased with increasing temperature, which does not satisfy the classical theory of thermal quenching, likely due to the increased $Yb^{3+}$ absorption cross-section at elevated temperatures [22,24]. A general theoretical description of the green upconversion emission can be given by [22]:

$$I_{green} = B\left[1 - \exp\left(-\frac{h\nu}{kT}\right)\right]^{-2} \tag{2}$$

where $B$ is a constant, and $h\nu$ is the phonon energy participating in the multiphonon-assisted excitation. The dependence of green upconversion emissions on temperature fits well to Equation (2). The $I_{green}/I_{red}$ value increased with temperature, causing the color to turn from red to green with elevated temperature.

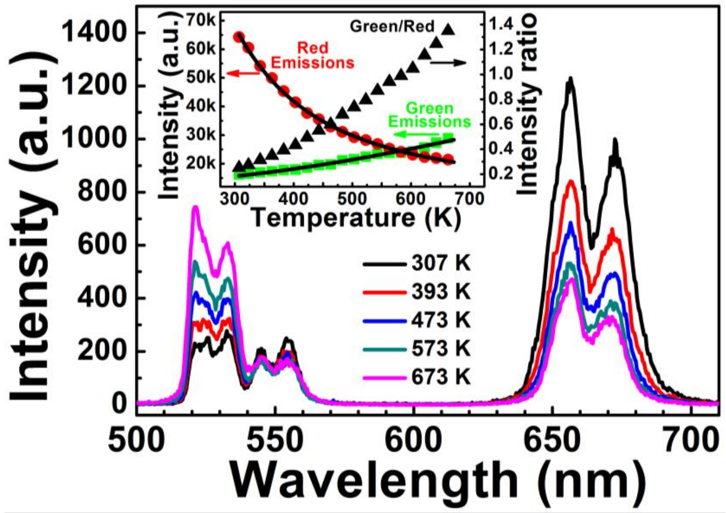

**Figure 4.** Upconversion emissions spectra of $Er^{3+}$-$Yb^{3+}$-$Mo^{6+}$-codoped $TiO_2$ at different temperatures. Inset shows the integrated intensity of green and red emissions and the intensity ratio of green to red emissions as a function of temperature. The solid lines for the temperature-dependent intensity of red and green emissions are fitting curves by Equations (1) and (2).

According to previous research [1], the relative population of two "thermally coupled" energy levels with separation of the order of thermal energy follows a Boltzmann-type population distribution, causing variation in the transitions of two closely spaced levels at elevated temperature if pumped through a continuous light source. After populations are thermalized at two closely spaced levels, the FIR of upconversion emissions ($R$) related to the transitions of both levels can be written as follows:

$$R = \frac{I_{\mathrm{upper}}}{I_{\mathrm{lower}}} = \frac{N_{\mathrm{upper}}}{N_{\mathrm{lower}}} = C\exp\left(\frac{-\Delta E}{kT}\right) \tag{3}$$

where $I_{\mathrm{upper}}$, $I_{\mathrm{lower}}$, $N_{\mathrm{upper}}$, and $N_{\mathrm{lower}}$ are the fluorescence intensity and number of ions for the upper and lower thermalizing energy levels, respectively; $\Delta E$ is the energy gap between two coupled levels, and $C$ is a constant relative to the degeneracy, emission cross-section, and angular frequency of corresponding transitions. Equation (3) suggests that FIR is related to the energy gap $\Delta E$ and temperature $T$. Figure 5 shows FIR plots of $(\mathrm{H_I} + \mathrm{H_{II}})/(\mathrm{S_I} + \mathrm{S_{II}})$, $\mathrm{H_I}/\mathrm{H_{II}}$, $\mathrm{S_I}/\mathrm{S_{II}}$, and $\mathrm{F_I}/\mathrm{F_{II}}$ as a function of inverse absolute temperature from 307 to 673 K. The inset shows corresponding upconversion emission intensity and the intensity ratio relative to temperature. The experimental data fits well to Equation (3). Energy gaps $\Delta E$ of the four coupled energy levels of $(H_I + H_{II})/(S_I + S_{II})$, $H_I/H_{II}$, $S_I/S_{II}$, and $F_I/F_{II}$ are calculated in Table 1. The decreased intensity of two red emissions with elevated temperature, shown in the inset of Figure 5d, can also be fitted to Equation (1). The activation energy of $F_I$ and $F_{II}$ levels is calculated as $\Delta E'_{FI} = 0.069$ eV and $\Delta E'_{FII} = 0.080$ eV, which is consistent with the average activation energy of $(F_I + F_{II})$ level ($\Delta E'_{(FI+FII)} = 0.074$ eV) shown in Figure 4.

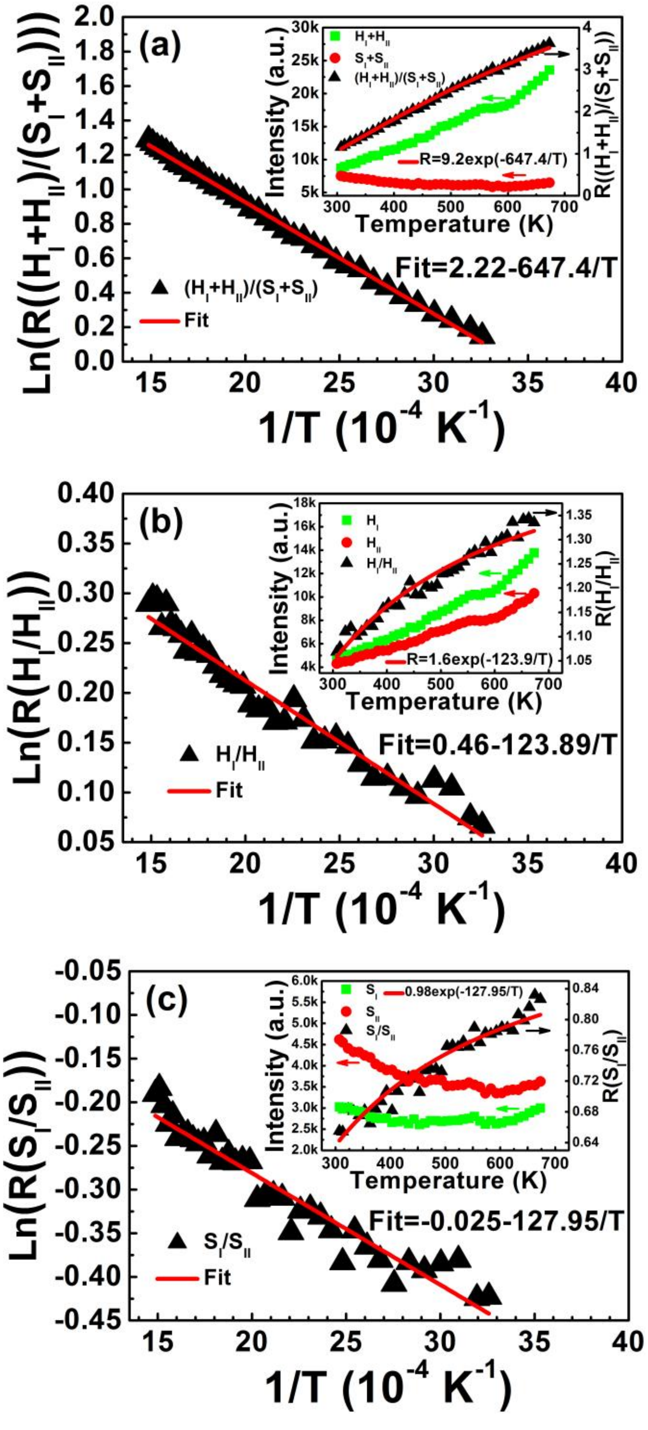

**Figure 5.** *Cont.*

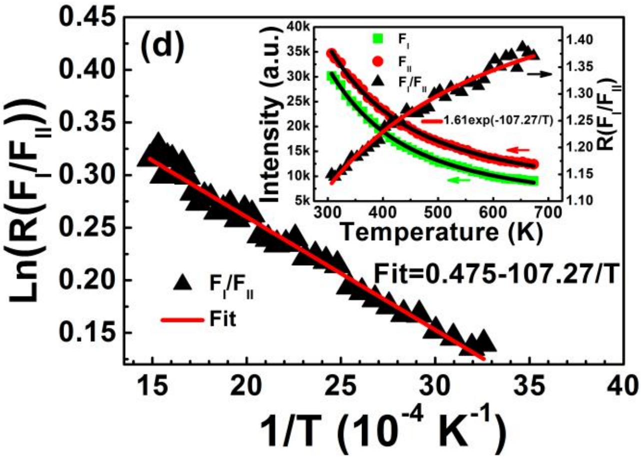

**Figure 5.** FIR plots of (**a**) ($H_I$ + $H_{II}$)/($S_I$ + $S_{II}$); (**b**) $H_I/H_{II}$; (**c**) $S_I/S_{II}$; and (**d**) $F_I/F_{II}$ as a function of inverse temperature in the range of 307–673 K. Insets show corresponding upconversion emission intensity and intensity ratio relative to temperature. FIR plots are fitted by Equation (3) and the temperature-dependent intensities of red emissions in (**d**) are fitted by Equation (1).

**Table 1.** Energy gap of coupled energy levels $\Delta E$, pre-exponential factor $C$, maximum sensitivity $S_{\max}$, temperature of maximum sensitivity $T_{\max}$ and upconversion emission intensity for the four coupled energy levels of ($H_I$ + $H_{II}$)/($S_I$ + $S_{II}$), $H_I/H_{II}$, $S_I/S_{II}$ and $F_I/F_{II}$.

| **Coupled Energy Levels** | **($H_I$ + $H_{II}$)/($S_I$ + $S_{II}$)** | **$H_I/H_{II}$** | **$S_I/S_{II}$** | **$F_I/F_{II}$** |
|---|---|---|---|---|
| $\Delta E$ (eV) | 0.0558 | 0.0107 | 0.0110 | 0.0093 |
| $C$ | 9.2 | 1.6 | 0.98 | 1.61 |
| $S_{\max}$ ($10^{-4}\cdot K^{-1}$) | 76.7 | 69.7 | 41.4 | 81.0 |
| $T_{\max}$ (K) | 324 | 62 | 64 | 54 |
| Upconversion intensity | Higher | Higher | Low | Highest |

For optical temperature-sensing applications, it is crucial to know the rate at which the FIR changes with temperature, known as the absolute sensitivity $S_a$, which is expressed as follows [1]:

$$S_a = \frac{1}{R}\frac{dR}{dT} = \frac{\Delta E}{kT^2} \tag{4}$$

Equation (4) makes clear that the appropriate selection of two thermally coupled energy levels with a suitable energy difference $\Delta E$ is very important. Larger $\Delta E$ benefits absolute sensitivity and accurate measurement of emission intensity, due to the decrease of fluorescence peak overlap originating from the two individual thermally coupled energy levels. Knowing this, the absolute sensitivity $S_a$ when using coupled energy levels of ($H_I$ + $H_{II}$)/($S_I$ + $S_{II}$) (with the largest possible $\Delta E$ = 0.0558 eV) is higher than those using the other three coupled levels, as shown in Table 1. The energy gap $\Delta E$ must be not too large, though, or thermalization no longer occurs.

Considering practical applications, it is extremely useful to be aware of variations in sensitivity with temperature. Relative sensitivity $S_r$ is expressed [25]:

$$S_r = \frac{dR}{dT} = R\frac{\Delta E}{kT^2} \tag{5}$$

Compared to absolute sensitivity $S_a$, relative sensitivity $S_r$ is dependent on not only energy gap $\Delta E$, but also the intensity ratio FIR. Equation (3) indicates that larger FIR causes larger $C$. Thus, larger $\Delta E$ and FIR (or $C$) contribute to higher $S_r$. Table 1 also shows pre-exponential factor $C$ values for the four pair energy levels ($H_I$ + $H_{II}$)/($S_I$ + $S_{II}$), $H_I/H_{II}$, $S_I/S_{II}$, and $F_I/F_{II}$. The coupled energy levels of

($H_I$ + $H_{II}$)/($S_I$ + $S_{II}$) processed larger relative sensitivity $S_r$ than those of $H_I/H_{II}$, $F_I/F_{II}$, or $S_I/S_{II}$. $S_r$ as a function of temperature for the four coupled energy levels calculated by Equation (5) is shown in Figure 6, in accordance with the above results in the measured temperature range 307–673 K.

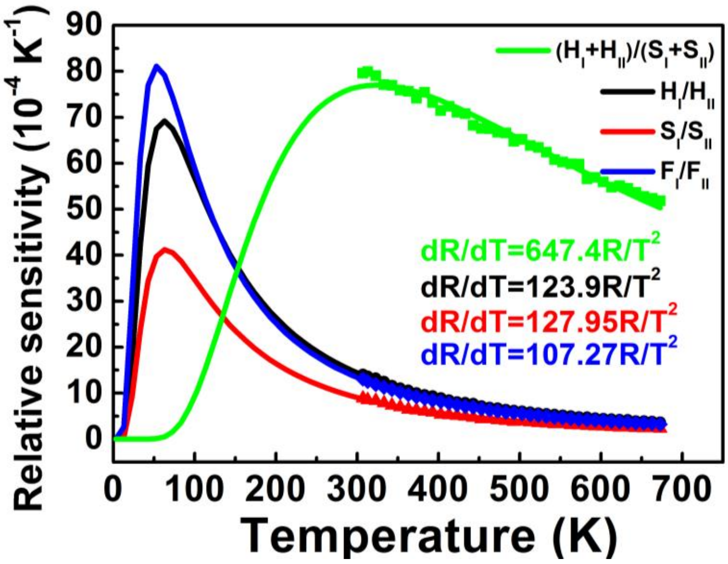

**Figure 6.** Relative sensitivities $S_r$ as a function of temperature for the four coupled energy levels of ($H_I$ + $H_{II}$)/($S_I$ + $S_{II}$), $H_I/H_{II}$, $S_I/S_{II}$ and $F_I/F_{II}$. Closed symbols are the experimental data and the lines are the theoretical values calculated by Equation (5).

Maximum sensitivity $S_{\max}$ and temperature $T_{\max}$, at which the sensor has maximum sensitivity $S_{\max}$, are of utmost importance because these two parameters indicate the highest sensitivity properties and optimum operating temperature range of optical thermal sensors. According to Equation (5), $S_{\max}$ and $T_{\max}$ can be calculated by $dS_r/dT = 0$ as follows:

$$S_{\max} = \frac{0.54C}{\Delta E/k} \tag{6}$$

$$T_{\max} = \frac{1}{2}\frac{\Delta E}{k} \tag{7}$$

Equation (6) indicates that a larger pre-exponential factor $C$ and smaller energy difference $\Delta E$ of coupled energy levels help to increase $S_{\max}$. Equation (7) shows that $T_{\max}$ is relative to the energy difference $\Delta E$, in which the sensor with a larger $\Delta E$ has a higher $T_{\max}$. $S_{\max}$ and $T_{\max}$ for the four coupled energy levels are shown in Table 1. The highest $T_{\max}$ was found for ($H_I$ + $H_{II}$)/($S_I$ + $S_{II}$) coupled energy levels used for thermal sensing, due to a larger $\Delta E$. The relatively larger $C$ and smallest $\Delta E$ in $F_I/F_{II}$ coupled energy levels used for thermal sensing resulted in the highest sensitivity $S_{\max}$.

Temperature measurement error can be calculated using the relation [8,26]:

$$\Delta T = \Delta R \frac{kT^2}{R\Delta E} = \frac{\Delta R}{S_r} \tag{8}$$

Larger $S_r$ and smaller $\Delta R$ imply better accuracy. As shown in Figure 6, larger $S_r$ at a higher temperature for coupled energy levels of ($H_I$ + $H_{II}$)/($S_I$ + $S_{II}$) led to a better accuracy in the high temperature range. Likewise, better accuracy can be expected in the low temperature range using $H_I/H_{II}$, $S_I/S_{II}$ and $F_I/F_{II}$ coupled energy levels for thermal sensing.

The separation of two coupled energy levels $\Delta E$ should be large enough to avoid overlap of the two fluorescence emissions and to produce efficient luminescence for feasible and accurate intensity measurement. The efficient luminescence of $Er^{3+}$-doped materials also contributes to the ready detection of luminescence and $\Delta R$ accuracy, where only low excitation power is needed. Table 1 shows where $(H_I + H_{II})/(S_I + S_{II})$ coupled energy levels had the highest accuracy of all samples, due to a larger $\Delta E$ and the strongest luminescence intensity; conversely, $S_I/S_{II}$ coupled energy levels had the lowest accuracy, evidenced by a smaller $\Delta E$ and the lowest luminescence intensity, which are altogether consistent with the results shown in Figure 5.

## 4. Conclusions

The green and red upconversion emissions by transitions of $Er^{3+}$ Stark sublevels were observed in $Er^{3+}$-$Yb^{3+}$-$Mo^{6+}$-codoped $TiO_2$ phosphors in this study. There are four coupled energy levels of $Er^{3+}$ ions due to the effect of the crystal field environment on $Er^{3+}$, each of which was utilized to study temperature-dependent upconversion emission properties. Based on the FIR technique, the optical temperature-sensing behaviors of sensing sensitivity, measurement error, and operating temperature for the four coupled energy levels were discussed in detail, with all closely related to the energy gap of the coupled energy levels, FIR value, and luminescence intensity. High sensitivity and negligible error are obtainable through the use of different coupled energy levels for optical sensing, throughout a wide range of temperature in an independent system. The utilization of coupled energy levels by Stark split is a new and effective method in the realization of multiple optical temperature measurement.

**Acknowledgments:** This work was supported by the National Natural Science Foundation of China (Grant No 11004021, 11204024, 11274057, and 11474046), Natural Science Foundation of Liaoning Province (Grant No. 2013020089), Program for Liaoning Excellent Talents in University, and Fundamental Research Funds for the Central Universities (Grant No. DC201502080202 and DC201502080406).

**Author Contributions:** This work was carried out in collaboration between all authors. Baosheng Cao, Jinlei Wu, Xuehan Wang and Zhiqing Feng carried out the experiments and analyzed the data. Baosheng Cao, Yangyang He and Bin Dong interpreted the results and wrote the paper. Baosheng Cao, Jinlei Wu, Xuehan Wang and Zhiqing Feng were involved in the experimental design, data acquisition and revision of the manuscript. All of the authors have read and approved the final version of the manuscript.

**Conflicts of Interest:** The authors declare no conflict of interest.

## References

1. Wade, S.A.; Collins, S.F.; Baxter, G.W. Fluorescence intensity ratio technique for optical fiber point temperature sensing. *J. Appl. Phys.* **2003**, *94*, 4743–4756. [CrossRef]
2. Wolfbeis, O.S. An overview of nanoparticles commonly used in fluorescent bioimaging. *Chem. Soc. Rev.* **2015**, *44*, 4743–4768. [CrossRef] [PubMed]
3. Wade, S.A.; Collins, S.F.; Baxter, G.W.; Monnom, G. Effect of strain on temperature measurements using the fluorescence intensity ratio technique (with $Nd^{3+}$- and $Yb^{3+}$-doped silica fibers). *Rev. Sci. Instrum.* **2001**, *72*, 3180–3185. [CrossRef]
4. Khalid, A.H.; Kontis, K. Thermographic phosphors for high temperature measurements: Principles, current state of the art and recent applications. *Sensors* **2008**, *8*, 5673–5744. [CrossRef]
5. Sidiroglou, F.; Wade, S.A.; Dragomir, N.M.; Baxter, G.W.; Collins, S.F. Effects of high-temperature heat treatment on $Nd^{3+}$-doped optical fibers for use in fluorescence intensity ratio based temperature sensing. *Rev. Sci. Instrum.* **2003**, *74*, 3524–3530. [CrossRef]
6. Schartner, E.P.; Monro, T.M. Fibre tip sensors for localised temperature sensing based on rare earth-doped glass coatings. *Sensors* **2014**, 21693–21701. [CrossRef] [PubMed]
7. Hao, S.W.; Chen, G.Y.; Yang, C.H. Sensing using rare-earth-doped upconversion nanoparticles. *Theranostics* **2013**, *3*, 331–345. [CrossRef] [PubMed]

8. Xu, W.; Zhao, H.; Li, Y.X.; Zheng, L.J.; Zhang, Z.G.; Cao, W.W. Optical temperature sensing through the upconversion luminescence from $Ho^{3+}/Yb^{3+}$ cdoped $CaWO_4$. *Sens. Actuators B Chem.* **2013**, *188*, 1096–1100. [CrossRef]
9. Cao, B.S.; Wu, J.L.; Feng, Z.Q.; Dong, B. Investigation of near-infrared-to-ultraviolet upconversion luminescence of $Tm^{3+}$ doped $NaYF_4$ phosphors by $Yb^{3+}$ codoping. *Mater. Chem. Phys.* **2013**, *142*, 333–338. [CrossRef]
10. Dong, B.; Liu, D.P.; Wang, X.J.; Yang, T.; Miao, S.M.; Li, C.R. Optical thermometry through infrared excited green upconversion emissions in $Er^{3+}$-$Yb^{3+}$ codoped $Al_2O_3$. *Appl. Phys. Lett.* **2007**, *90*. [CrossRef]
11. Wang, X.; Kong, X.; Yu, Y.; Sun, Y.; Zhang, H. Effect of annealing on upconversion luminescence of $ZnO:Er^{3+}$ nanocrystals and high thermal sensitivity. *J. Phys. Chem. C* **2007**, *111*, 15119–15124. [CrossRef]
12. Cao, B.S.; He, Y.Y.; Zhang, L.; Dong, B. Upconversion properties of $Er^{3+}$-$Yb^{3+}$: $NaYF_4$ phosphors with a wide range of $Yb^{3+}$ concentration. *J. Lumin.* **2013**, *135*, 128–132. [CrossRef]
13. Vetrone, F.; Naccache, R.; Zamarron, A.; de la Fuente, A.J.; Sanz-Rodriguez, F.; Maestro, L.M.; Rodriguez, E.M.; Jaque, D.; Sole, J.G.; Capobianco, J.A. Temperature sensing using fluorescent nanothermometers. *ACS Nano* **2010**, *4*, 3254–3258. [CrossRef] [PubMed]
14. Cao, B.S.; He, Y.Y.; Sun, Y.; Song, M.; Dong, B. Optical high temperature sensor based on enhanced green upconversion emissions in $Er^{3+}$-$Yb^{3+}$-$Li^{+}$ codoped $TiO_2$ powders. *J. Nanosci. Nanotechnol.* **2011**, *11*, 9899–9903. [CrossRef] [PubMed]
15. Soni, A.K.; Dey, R.; Rai, V.K. Stark sublevels in $Tm^{3+}$-$Yb^{3+}$ codoped $Na_2Y_2B_2O_7$ nanophosphor for multifunctional applications. *RSC Adv.* **2015**, *5*, 34999–35009. [CrossRef]
16. Rai, V.K.; Rai, S.B. Temperature sensing behaviour of the stark sublevels. *Spectrochim. Acta A* **2007**, *68*, 1406–1409. [CrossRef] [PubMed]
17. Baxter, G.W.; Maurice, E.; Monnom, G. Thermal variation of absorption in $Yb^{3+}$-doped silica fiber for high-temperature sensor applications. *Proc. SPIE* **1995**, *2510*, 293–296.
18. Feng, Z.J.; Zhang, X.S.; Zhou, Y.L.; Ling, Z.; Li, M.Z.; Sun, J.; Li, L. Influence of temperature on the transition of Stark sublevels of $Er^{3+}$ doped ZBLAN glass. *Acta Opt. Sin.* **2013**, *33*. [CrossRef]
19. Cao, B.S.; Wu, J.L.; Yu, N.S.; Feng, Z.Q.; Dong, B. Structure and upconversion luminescence properties of $Er^{3+}$-$Mo^{6+}$ codoped $Yb_2Ti_2O_7$ films. *Thin Solid Films* **2014**, *550*, 495–498. [CrossRef]
20. Dong, B.; Cao, B.S.; He, Y.Y.; Liu, Z.; Li, Z.P.; Feng, Z.Q. Temperature Sensing and *in Vivo* Imaging by Molybdenum Sensitized Visible Upconversion Luminescence of Rare-Earth Oxides. *Adv. Mater.* **2012**, *24*, 1987–1993. [CrossRef] [PubMed]
21. Cao, B.S.; He, Y.Y.; Feng, Z.Q.; Dong, B. Optical temperature sensing behavior of enhanced green upconversion emissions from Er-Mo:$Yb_2Ti_2O_7$ nanophosphor. *Sens. Actuators B Chem.* **2011**, *159*, 8–11. [CrossRef]
22. Cao, B.S.; Wu, J.L.; Wang, X.H.; He, Y.Y.; Feng, Z.Q.; Dong, B.; Rino, L. Multiple temperature effects on up-conversion fluorescences of $Er^{3+}$-$Yb^{3+}$-$Mo^{6+}$ codoped $TiO_2$ and high thermal sensitivity. *AIP Adv.* **2015**, *5*. [CrossRef]
23. Chen, Y.H.; Liu, B.; Shi, C.S.; Ren, G.H.; Zimmerer, G. The temperature effect of $Lu_2SiO_5$: $Ce^{3+}$ luminescence. *Nucl. Instrum. Methods. A* **2005**, *537*, 31–35. [CrossRef]
24. Zhou, S.Q.; Li, C.R.; Liu, Z.F.; Li, S.F.; Song, C.L. Thermal effect on up-conversion in $Er^{3+}/Yb^{3+}$ co-doped silicate glass. *Opt. Mater.* **2007**, *30*, 513–516. [CrossRef]
25. Singh, S.K.; Kumar, K.; Rai, S.B. $Er^{3+}/Yb^{3+}$ codoped $Gd_2O_3$ nano-phosphor for optical thermometry. *Sens. Actuators A Phys.* **2009**, *149*, 16–20. [CrossRef]
26. Tripathi, G.; Rai, V.K.; Rai, S.B. Upconversion and temperature sensing behavior of $Er^{3+}$ doped $Bi_2O_3$-$Li_2O$-BaO-PbO tertiary glass. *Opt. Mater.* **2007**, *30*, 201–206. [CrossRef]

© 2015 by the authors; licensee MDPI, Basel, Switzerland. This article is an open access article distributed under the terms and conditions of the Creative Commons by Attribution (CC-BY) license (http://creativecommons.org/licenses/by/4.0/).